LIMITS ON THE MASS OF THE CENTRAL BLACK HOLE IN 16 NEARBY BULGES[1]

MARC SARZI,[2,3] HANS-WALTER RIX,[2] JOSEPH C. SHIELDS,[4] DANIEL H. MCINTOSH,[5] LUIS C. HO,[6] GREGORY RUDNICK,[2,7] ALEXEI V. FILIPPENKO,[8] WALLACE L. W. SARGENT,[9] AND AARON J. BARTH[10]

ABSTRACT

We report upper limits on the masses of black holes that can be present in the centers of 16 nearby galaxy bulges. These limits $M_{\rm BH}^{\rm lim}$ for our statistically complete sample were derived from the modeling of the central emission-line widths ([N II] or [S II]), observed over a $0\farcs25 \times 0\farcs2$ ($R \lesssim 9$ pc) aperture. The experiment has a mean detection sensitivity of $\sim 3.9 \times 10^6 \ M_\odot$. For three sample members with direct determinations of $M_{\rm BH}$ our upper limits agree within the uncertainties, while in general our upper limits are found to be close to the masses measured in other bulges with global properties similar to ours. Remarkably, our limits are quite close to the recently derived $M_{\rm BH}$-σ_* relation. These results support a picture wherein the black hole mass and overall galaxy structure are closely linked, as galaxies with exceptionally high $M_{\rm BH}$ at a given σ_* apparently are rare.

Subject headings: galaxies: bulges — galaxies: kinematics and dynamics — galaxies: nuclei — galaxies: spiral

1. INTRODUCTION

The last few years have seen great progress in studying the dark mass concentrations at the centers of "ordinary" quiescent galaxies, showing that they are very common and demonstrating in some cases that they must be supermassive black holes (SMBHs) by ruling out all astrophysically viable alternatives. Indeed, a picture is emerging in which SMBHs in the range of 10^6–$10^9 \ M_\odot$ are an integral part of galaxy formation (e.g., Kauffmann & Haehnelt 2000). Two examples in the local universe stand out with particularly convincing evidence as SMBHs: the Milky Way and NGC 4258. At the Galactic center, direct observations of individual stars (Genzel et al. 1997; Eckart & Genzel 1997; Ghez et al. 1998) and a stream of ionized gas (Herbst et al. 1993) orbiting Sgr A* show that all the dynamically relevant mass inside ~ 1 pc, $2.6 \times 10^6 \ M_\odot$, is concentrated with a density of $\rho > 10^{12} \ M_\odot$ pc^{-3}. In NGC 4258, a disk of masing molecular gas is orbiting the center with a Keplerian rotation curve as traced by H_2O maser emission (Miyoshi et al. 1995); models imply that $M_{\rm BH} \approx 3.6 \times 10^7 \ M_\odot$ and $\rho > 4 \times 10^9 \ M_\odot$ pc^{-3}. Alternatives to SMBHs, such as clusters of brown dwarfs or stellar remnants, can be ruled out in these two cases (e.g., Maoz 1995, 1998).

A number of techniques have matured that have demonstrated the presence of a central dark mass concentration in an ever growing number of nearby galaxy nuclei, with mass estimates accurate to a factor of ~ 2 and concentration limits of $\rho > 10^6$–$10^8 \ M_\odot$ pc^{-3}. Simple analogy with the exemplary cases in which the SMBH presence is all but proven and the connection to active galactic nucleus (AGN) activity at various intensity levels suggest strongly that these central dark masses are SMBHs as well. The most widely used technique is stellar dynamical modeling (e.g., Dressler & Richstone 1988; Kormendy et al. 1996a, 1996b; van der Marel et al. 1997; Cretton & van den Bosch 1999; Gebhardt et al. 2000a), which has provided mass estimates for over two dozen nuclei, mostly in massive, early-type galaxies. Modeling the kinematics of ionized gas has produced a number of additional mass measurements (e.g., Harms et al. 1994; Ferrarese, Ford, & Jaffe 1996; Bower et al. 1998; Verdoes Kleijn et al. 2000; Sarzi et al. 2001, hereafter S01; Barth et al. 2001a). Finally, application of results from reverberation mapping of AGNs has yielded central virial mass estimates for Seyfert galaxies (Ho 1999; Wandel, Peterson, & Malkan 1999) and QSOs (Kaspi et al. 2000) that seem to be robust (Gebhardt et al. 2000b; Ferrarese et al. 2001).

Taken together, these results show that $M_{\rm BH}$ is correlated both with the stellar luminosity (Kormendy & Richstone 1995; Magorrian et al. 1998; Ho 1999) and, more tightly, with the velocity dispersion of the bulge (Gebhardt et al. 2000a; Ferrarese & Merritt 2000). By contrast, $M_{\rm BH}$ is unrelated to the properties of galaxy disks. The growth of SMBHs appears to be closely linked with the formation of bulges. However, the actual slope and scatter of the $M_{\rm BH}$-$L_{\rm bulge}$ and $M_{\rm BH}$-σ_* relations are still under debate. It is also important to remember that our knowledge about SMBHs is very uneven across the Hubble sequence of galaxies. The existing samples are preferentially weighted toward early-type galaxies with very massive black holes. From an observational point of view, there is a pressing need to acquire better $M_{\rm BH}$ statistics for spiral galaxies.

Motivated by the recent progress and the emerging correlations, but also by the desire to improve the black hole census in spirals, we derive mass constraints on SMBHs potentially present in the bulges of 16 nearby disk galaxies. As we will show, these constraints constitute significant progress, both in terms of the number of target galaxies and in terms of broadening the range of parent galaxies with significant constraints.

We draw on spectra of nearby nuclei obtained with the Space Telescope Imaging Spectrograph (STIS) on board the *Hubble Space Telescope* (*HST*), taken as part of the Spectroscopic Survey of Nearby Galaxy Nuclei (SUNNS) project (Shields et al. 2000; Ho et al. 2000; S01; H.-W. Rix et al. 2002, in preparation). Only four of our original 24 target galaxies showed extended line emission with symmetric kinematics and hence were suited for a direct M_{BH} determination. These cases have been modeled by S01 and yielded M_{BH} estimates. Here we analyze data for 16 galaxies from SUNNS with central [N II] $\lambda\lambda 6548$, 6583 and [S II] $\lambda\lambda 6716$, 6731 line emission from ionized gas. In most cases the central gas emission is spatially unresolved, or only marginally so, and has line widths $\sim 10^2$ km s^{-1}.

Spatially unresolved lines do not permit precise mass estimates but potentially do allow us to derive useful upper limits on M_{BH}. This is because the line emission in our central aperture must arise from gas at a distance from the center that is, at most, equal to the physical dimension of the region subtended by the central aperture itself, for our sample typically ~ 9 pc. If the gas motions are orbital, all velocities and hence the integrated line width will scale as $M_{BH}^{1/2}$. Note that the resulting limit on M_{BH} scales linearly with the central aperture size, affording *HST* an order-of-magnitude gain over ground-based observations (e.g., Salucci et al. 2000) and making the derived limits astrophysically interesting.

At parsec-scale distances from galactic centers the gas is subject not only to gravitational forces but also to gas pressure and magnetic forces (e.g., for the Milky Way, Timmermann et al. 1996; Yusef-Zadeh, Roberts, & Wardle 1997). In general, these other effects cause additional line broadening.

The paper is organized as follows. In § 2 we present the spectroscopic and photometric STIS observations, and in § 3 we describe our modeling of the ionized gas kinematics. In §§ 4 and 5 we present our results and draw our conclusions.

2. OBSERVATIONS AND DATA REDUCTION

2.1. *Galaxy Sample*

All sample galaxies, mostly early-type disk galaxies (S0–Sb), were observed with STIS as part of the SUNNS project; the full details of this program will be reported elsewhere (H.-W. Rix et al. 2002, in preparation). The SUNNS galaxies are drawn from the Palomar spectroscopic survey of nearby galaxies (Filippenko & Sargent 1985; Ho, Filippenko, & Sargent 1995, 1997) and include all S0–Sb galaxies within 17 Mpc known to have line emission ($\gtrsim 10^{15}$ ergs s^{-1} cm^{-2}) within a $2'' \times 4''$ aperture. The present sample constitutes the subset of SUNNS objects with sufficient central line flux in Hα or [N II] to provide adequate signal-to-noise ratio (S/N $\gtrsim 10$). With the experimental setup described below, the sample is effectively defined by galaxies that have Hα or [N II] line fluxes $\gtrsim$ 10^{-14} ergs s^{-1} cm^{-2} within a 0.25×0.2 central aperture,

which correspond to line luminosities of $\gtrsim 3 \times 10^{38}$ ergs s^{-1} at the mean sample distance of 15 Mpc.

Our sample is statistically well defined and complete in the sense that the original SUNNS sample was a volume-limited sample selected by emission-line flux within a (much larger) $2'' \times 4''$ aperture. The basic parameters of the target galaxies are given in Table 1.

2.2. *Observations*

HST observations were acquired for all objects in SUNNS during 1998 and 1999. We placed the $0.2 \times 52''$ slit across each nucleus along an operationally determined position angle, which is effectively random with respect to the galaxy orientation. After initial 20 s acquisition exposures with the optical long-pass filter (roughly equivalent to *R*), from which we derive surface photometry of the central regions, three exposures totaling approximately 45 minutes were obtained with the G750M grating; this resulted in spectra that cover 6300–6850 Å with an FWHM resolution for extended sources of 1.6 Å.

For nine of the 16 galaxies in the present sample, the telescope was offset by 0.05 (~ 1 pixel) along the slit between repeated exposures to aid in the removal of hot pixels and cosmic rays. The two-dimensional spectra were bias- and dark-subtracted, flat-fielded, aligned, and combined into single frames. Cosmic rays and hot pixels remaining in the combined two-dimensional spectra were cleaned following the recipe of Rudnick, Rix, & Kennicutt (2000). The two-dimensional spectra were then corrected for geometrical distortion and then wavelength and flux calibrated with standard STSDAS procedures within IRAF.[11]

To represent the generic "nuclear spectrum" of each galaxy, we extracted aperture spectra 5 pixels wide (~ 0.25), centered on the brightest part of the continuum. The acquisition images indicate that the uncertainties in the galaxy center due to dust are $\lesssim 0.25$ pixels ~ 0.012 (see also S01). In essence, therefore, the extracted spectra represent the average central emission, convolved with the STIS spatial point-spread function (PSF) and sampled over an aperture of 0.25×0.2, or 18 pc $\times$ 14 pc for the mean sample distance of 15 Mpc.

For three of our galaxies, central stellar velocity dispersions were either not available in the literature (NGC 3992 and NGC 4800) or quite uncertain (NGC 3982; Nelson & Whittle 1995). Therefore, we obtained new spectroscopic data for these objects on two observing runs: with the Boller & Chivens spectrograph at the Bok 90 inch telescope in 2000 May for NGC 3992, and with the Double Spectrograph (Oke & Gunn 1982) at the Palomar 200 inch telescope in 2001 June for NGC 3982 and NGC 4800. At Kitt Peak we used the 600 groove mm^{-1} grating to cover 3600–5700 Å with a pixel scale on the CCD of 1.86 Å pixel^{-1}, while for the Palomar run we observed the Ca infrared triplet using the 1200 groove mm^{-1} grating on the red side of the Double Spectrograph, with a pixel scale of 0.63 Å pixel^{-1}. Spectra were extracted for apertures of 3.3×2.5 and 3.7×2.0 for the Bok and Palomar spectra, respectively. Total exposure times were 40, 30, and 60 minutes for NGC 3982, NGC 3992, and NGC 4800, respectively. The stellar velocity dispersions were measured following the

---

TABLE 1

BASIC PARAMETERS OF THE SAMPLE GALAXIES

Galaxy (1)	Hubble Type (2)	B_T (mag) (3)	Spectral Class (4)	D (Mpc) (5)	σ_* (km s^{-1}) (6)	Reference (7)	σ_e (km s^{-1}) (8)	σ_{cen} (km s^{-1}) (9)	Observation Date (10)
NGC 2787......	SB0$^+$	11.82	L1.9	13.0	210 ± 23	1	185 ± 20	215.1 ± 4.3	1998 Dec 05
NGC 3351......	SBb	10.53	H	8.1	101 ± 16	2	93 ± 15	47.2 ± 1.5	1998 Dec 25
NGC 3368......	SABab	10.11	L2	8.1	135 ± 10	3	114 ± 8	101.5 ± 3.1	1998 Oct 31
NGC 3982......	SABb:	...	S1.9	17.0	78 ± 2	4	78 ± 2	136.7 ± 3.5	1998 Apr 11
NGC 3992......	SBbc	10.60	T2:	17.0	140 ± 20	4	119 ± 17	109.5 ± 3.1	1999 Feb 19
NGC 4143......	SAB0°	11.65	L1.9	17.0	270 ± 12	5	271 ± 12	226.3 ± 2.1	1999 Mar 20
NGC 4203......	SAB0$^-$:	11.80	L1.9	9.7	124 ± 16	1	110 ± 14	148.9 ± 5.2	1999 Apr 18
NGC 4321......	SABbc	10.05	T2	16.8	83 ± 12	6	74 ± 11	85.7 ± 1.7	1999 Apr 23
NGC 4450......	Sab	10.90	L1.9	16.8	130 ± 17	2	121 ± 16	162.4 ± 1.7	1999 Jan 31
NGC 4459......	S0$^+$	11.32	T2:	16.8	189 ± 21	1	167 ± 18	193.1 ± 5.2	1999 Apr 23
NGC 4477......	SB0:?	11.38	S2	16.8	156 ± 12	7	134 ± 10	128.9 ± 2.2	1999 Apr 23
NGC 4501......	Sb	10.36	S2	16.8	151 ± 17	8	136 ± 15	110.8 ± 1.8	1999 Apr 26
NGC 4548......	SBb	10.96	L2	16.8	82 ± 9	9	71 ± 8	81.2 ± 1.8	1999 Apr 26
NGC 4596......	SB0$^+$	11.35	L2::	16.8	154 ± 5	10	136 ± 4	142.0 ± 8.7	1998 Dec 20
NGC 4698......	Sab	11.46	S2	16.8	134 ± 6	9	116 ± 5	101.9 ± 2.2	1997 Nov 24
NGC 4800......	Sb	12.30	H	15.2	112 ± 2	4	112 ± 2	71.9 ± 7.0	1999 Mar 03

NOTE.—Col. (1): Galaxy name. Col. (2): Hubble type from de Vaucouleurs et al. 1991. Col. (3): Total apparent B magnitude from de Vaucouleurs et al. 1991. Col. (4): Nuclear spectral class from Ho et al. 1997, where H = H II nucleus, L = LINER, S = Seyfert, T = "transition object" (LINER/H II), 1 = type 1, 2 = type 2, and a fractional number between 1 and 2 denotes various intermediate types; uncertain and highly uncertain classifications are followed by a single and double colon, respectively. Col. (5): Distance from Tully 1988, who assumes $H_0 = 75$ km s^{-1} Mpc^{-1}. Col. (6): Ground-based central stellar velocity dispersion σ_*. Col. (7): Reference for σ_*. Col. (8): Stellar velocity dispersion within one effective radius σ_e, derived from the σ_* value following the extrapolation of Jørgensen et al. 1995. Col. (9): Measured gas velocity dispersion within the central $0\rlap{.}''25 \times 0\rlap{.}''2$. Col. (10): UT observation date.

REFERENCES.—(1) Dalle Ore et al. 1991. (2) Whitmore, Schechter, & Kirshner 1979. (3) Héraudeau et al. 1999. (4) This paper (§ 2.2). (5) Di Nella et al. 1995. (6) Schechter 1983. (7) Jarvis et al. 1988. (8) Héraudeau & Simien 1998. (9) Corsini et al. 1999. (10) Kent 1990.

method of Rix et al. (1995), and the obtained values are reported in Table 1.

2.3. *Central Emission-Line Widths and Flux Profiles*

To quantify the emission-line velocity widths in these nuclear spectra, we simultaneously fitted Gaussians of single width σ_{cen} to the [N II] $\lambda\lambda 6548, 6583$ and [S II]

$\lambda\lambda 6716, 6731$ emission-line doublets, using the IRAF task SPECFIT. The profiles of the [N II] and [S II] lines were found to be roughly Gaussian. We restricted ourselves to line widths from forbidden transitions to sidestep the impact of a possible broad (broad-line region) component arising from radii much smaller than our observational aperture. However, in all objects where only a narrow Hα
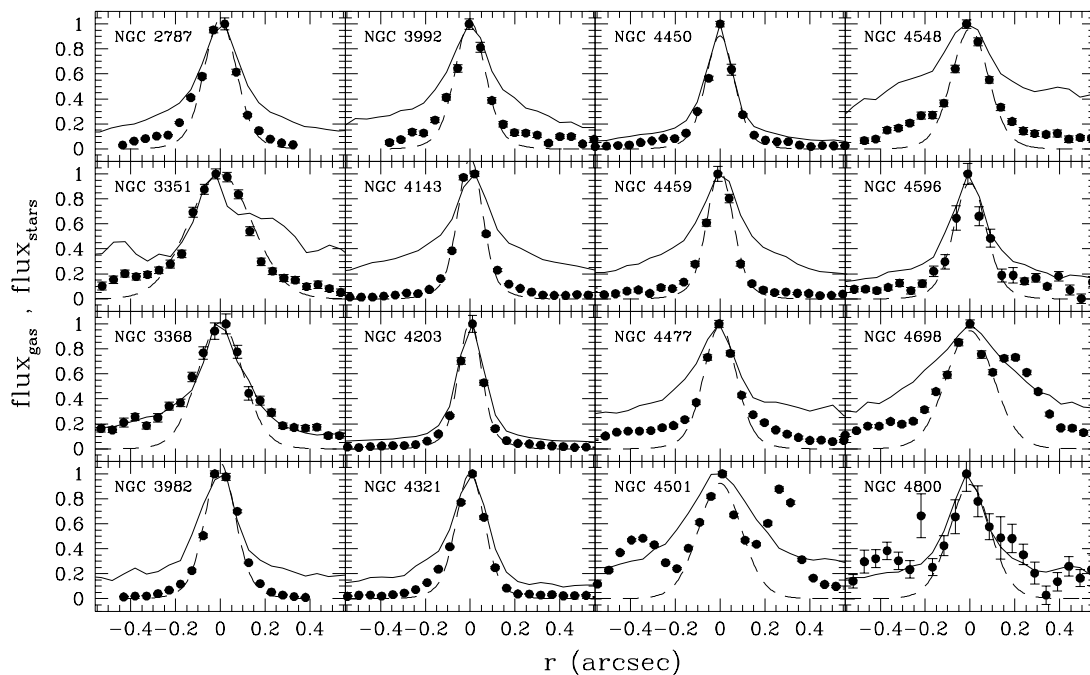

FIG. 1.—Observed emission-line flux profiles along the direction of the STIS slit. In each panel the filled symbols represent the observed [N II] fluxes at each CCD row along the slit (corresponding to a synthesized aperture of $0\rlap{.}''05 \times 0\rlap{.}''2$), while the dashed line shows the fit to the central five points as described in § 3.2. For comparison the solid line represents the stellar continuum profile, extracted from the region free of emission lines between 6536 and 6542 Å. Both emission-line and continuum flux profiles have been rescaled so that their peak values equal unity.

emission line component was present, we also included Hα in the fit. In the few cases with prominent, very broad Hα lines (e.g., NGC 4203, Shields et al. 2000; NGC 4450, Ho et al. 2000), particular care was taken to minimize the impact of the very broad lines on the estimate of $\sigma_{\rm cen}$ in the adjacent [N II] lines. In virtually all objects the S/N is in excess of 10, and hence the formal errors in the estimated line width are negligible for the subsequent analysis. The instrumental line width derived from comparison lamps is $\sigma_{\rm inst} \approx 32$ km s^{-1} and was subtracted from the raw measurement of $\sigma_{\rm cen}$ in quadrature; for all but two objects these line width corrections were negligible, implying that the intrinsic widths were well resolved. This correction also spares us from accounting in the following modeling of the line width for the broadening due to the instrumental line-spread function. The resulting values for $\sigma_{\rm cen}$ are listed in Table 1. Their characteristic errors, including the correction for the instrumental line width, are less than 10 km s^{-1}.

As we will detail below, any information on the gas spatial flux distribution on scales $\lesssim 0\farcs25$ provides a valuable constraint for the central line width modeling procedure. Therefore, we also obtained radial profiles along the slit direction for the ionized gas flux, by fitting a Gaussian to the [N II] $\lambda 6583$ line flux profile along the spatial direction on the two-dimensional spectra. We chose [N II] because among our sample galaxies this is almost always the brightest line and because it is less likely to be affected by underlying absorption features in the stellar continuum than Hα. The [N II] emission-line flux profiles are shown in Figure 1.

3. MODELING THE CENTRAL LINE WIDTH

3.1. Basic Concept

We are now faced with converting the observed central line widths into estimates for the central black hole mass. To start, we assume that the ionized gas motion is dominated solely by gravity. In this case the central line width depends on (1) the total gravitational potential of the putative SMBH and of the surrounding stars, (2) the spatial emissivity distribution (e.g., that of a disk inclined at cos i), and (3) the "kinematic behavior" of the ionized gas, for example, "dynamically cold" gas moving on circular orbits or hotter gas with hydrostatic support. The lack of spatially resolved information on the gas flux distribution within the central $0\farcs25 \times 0\farcs2$ aperture means that we can only derive upper limits to $M_{\rm BH}$; if the emission-line flux within the aperture arose from $R \ll R_{\rm aperture} \approx 0\farcs1$, arbitrarily small values of $M_{\rm BH}$ could explain the observed line width. If the gas motion is also affected by nongravitational forces, such as outflows, magnetic fields, or supernova winds, this would broaden the integrated line velocity width additionally and hence lower the required black hole mass needed to explain a given $\sigma_{\rm cen}$. By ignoring nongravitational forces we are therefore conservative in estimating upper limits for the central black hole mass. The absence of constraints on the importance of nongravitational forces constitutes a second reason (besides the lack of spatially resolved information on the gas flux) why it is not possible to secure the presence of an SMBH in our sample galaxies, as hypothetically the observed line widths could be entirely explained by nongravitational effects.

If the functional form of the potential well is fixed, then the central line width will scale with the potential for any

given choice of the emissivity distribution and for the gas kinematical behavior. In the simplest case of a purely Keplerian potential induced by an SMBH, $\Phi_{\rm BH}$, the expected central line width will scale as the square root of the black hole mass. As the circular velocity at any given reference radius $R_{\rm ref}$, $v_c(R_{\rm ref})$, will scale in the same way, the ratio between $\sigma_{\rm cen}$ and $v_c(R_{\rm ref})$ is independent of black hole mass. The task at hand is therefore to derive a plausible range of values for this ratio by varying the spatial emissivity distribution and then to obtain a mass range for the putative SMBH from the observed central line width via $\sigma_{\rm cen} \rightarrow v_c^2(R_{\rm ref}) \rightarrow M_{\rm BH} = v_c^2(R_{\rm ref})R_{\rm ref}/G$.

The same would hold for a sequence of purely stellar potentials derived from the luminosity density with differing mass-to-light ratios Υ. When both the stellar and the SMBH contributions to the gravitational potential are considered, the shape of the rotation curve, and hence $\sigma_{\rm cen}/v_c(R_{\rm ref})$, will depend on the relative weight of $M_{\rm BH}$ and Υ.

In all cases we will proceed through the following steps in order to make a prediction for the gas velocity dispersion within the central aperture:

1. Specify the spatial gas emissivity distribution and the gravitational potential and choose the kinematic behavior of the gas.

2. Construct two-dimensional maps for the moments of the line-of-sight velocity distribution (LOSVD) at any position (x, y) on the sky

$$\overline{\Sigma v^k}(x, y) = \int {\rm LOSVD}(x, y, v_z)v_z^k \, dv_z \quad (k = 0, 1, 2) , \quad (1)$$

as they would appear without the limitations of the spatial resolution; the first moment, for instance, is the mean gas velocity.

3. Convolve each of the two-dimensional $\overline{\Sigma v^k}$ maps with the STIS PSF.

4. Sample the convolved $\overline{\Sigma v^k_{\rm conv}}$ two-dimensional maps over the desired aperture to obtain the PSF-convolved, aperture-averaged LOSVD velocity moments $\overline{\Sigma v^k_{\rm conv,ap}}$, which are directly comparable to the observables.

5. In particular, compute the ionized gas flux $f_{\rm ap}$, the projected mean streaming velocity $\bar{v}_{\rm ap}$, and the velocity dispersion $\sigma_{\rm ap}$ within the desired aperture through $f_{\rm ap} = \overline{\Sigma v^0_{\rm conv,ap}}$, $\bar{v}_{\rm ap} = \overline{\Sigma v^1_{\rm conv,ap}}/f_{\rm ap}$, and $\sigma_{\rm ap} = (\overline{\Sigma v^2_{\rm conv,ap}}/f_{\rm ap} - \bar{v}_{\rm ap}^2)^{1/2}$, respectively. The last quantity, $\sigma_{\rm ap}$, can be compared with the measured velocity width $\sigma_{\rm cen}$.

In what follows, we will first derive upper limits on $M_{\rm BH}$ assuming that the gas is moving on circular orbits in a coplanar, randomly oriented disk within a Keplerian potential (§ 3.2); then we consider the impact of the stellar potential on this disk modeling (§ 3.3); finally, we will explore a seemingly very different situation for the kinematical behavior of the gas, that of hydrostatic equilibrium (§ 3.4), to demonstrate that our results are robust with respect to the underlying model assumptions. We anticipate that the most conservative upper limits on $M_{\rm BH}$ are derived from the first approach, where the impact of the stellar potential is neglected.

3.2. The Keplerian Disk Modeling

We start with the simple and plausible assumption that the ionized gas moves on circular orbits at the local circular

velocity, which in turn is dictated solely by the gravitational influence of the putative SMBH, $v_c^2(R) = GM_{\mathrm{BH}}/R$. We further assume that the gas resides in a coplanar disk of unknown inclination with an intrinsically axisymmetric emissivity distribution, $\Sigma(R)$, centered on the stellar nucleus. Our best guess for $\Sigma(R)$ is derived from the data themselves. In this Keplerian disk the LOSVD at each position (x, y) on the sky plane is just

$$\mathrm{LOSVD}(x, y, v_z) = \Sigma_{\mathrm{proj}}(x, y)\delta[v_{c,\mathrm{proj}}(x, y) - v_z] \quad (2)$$

and its $\overline{\Sigma v^k}$ velocity moments are simply given by $\Sigma_{\mathrm{proj}}(x, y)$, $\Sigma_{\mathrm{proj}}(x, y)v_{c,\mathrm{proj}}(x, y)$, and $\Sigma(x, y)v_{c,\mathrm{proj}}^2(x, y)$, respectively, where Σ_{proj} and $v_{c,\mathrm{proj}}$ are the projected gas surface brightness and circular velocity. To deal with the central circular velocity singularity, we neglected the contribution of the central point of the two-dimensional maps for the $\overline{\Sigma v^k}$ velocity moments, and we refined their grid sizes until no further substantial increase in the predicted line widths was found. The adopted grid size in our models corresponds to $0\farcs005$, or 0.1 pixels.

The geometry of the projected velocity field will depend on the disk orientation, specified by its inclination i with respect to the sky plane and its major axis position angle ϕ with respect to the slit direction. We have no information on the gas disk orientation within our central aperture, since the dust lane morphology we employed in S01 cannot be used to provide a constraint on such small scales. Therefore, we need to explore all possible disk orientations to derive the probability distribution for $\sigma_{\mathrm{ap}}/v_c(R_{\mathrm{ref}})$, the ratio between the predicted central velocity dispersion and the circular velocity at the reference radius. We adopt $R_{\mathrm{ref}} = 0\farcs125$, corresponding to the distance of the central aperture edge from the center along the slit direction. We cover the possible disk orientations by constructing a grid of models with equally spaced $\cos i$ and ϕ.

For the intrinsic radial surface brightness profile of the gas we assumed a Gaussian

$$\Sigma(R) = a_{\mathrm{flux}} e^{-R^2/2\sigma_{\mathrm{flux}}^2}, \quad (3)$$

and we derived a_{flux} and σ_{flux} by matching the observed emission flux profiles along the slit (see § 2.3). This match again involves convolving the intrinsic $\Sigma(R)$ with the STIS PSF, which we parameterized as a sum of Gaussian components (see S01). The choice of a Gaussian for the intrinsic surface brightness distribution was a matter of convenience, for the convolution process in this case is simply analytical. Intrinsically more concentrated profiles, such as exponential ones, would also reproduce the data once convolved with the STIS PSF and would lead to tighter upper limits on M_{BH}, which make our choice more conservative. We fit only the central five flux pixels for each galaxy, corresponding to the same region subtended by our central aperture.

Figure 1 displays our best fits of $\Sigma(R)$ and illustrates that our model (eq. [3]) matches the data well within less than $0\farcs125$ in all cases.[12] Table 2 lists the best-fitting σ_{flux} values. The actual position of the data points with respect to the center of the fitting function can be explained entirely by a small displacement ($\ll R_{\mathrm{ref}}$) of the slit center from that of the gaseous disk, without violating our assumption of an axisymmetric emissivity distribution. Including this small offset in the modeling produces only negligible variations in the predicted central σ_{ap}. In this case the predicted mean velocities $\bar{v}_{\mathrm{ap}}$, although nonzero, are very small, and conse-

---

[12] All [N II] flux profiles of Fig. 1 were symmetrical even outside the central aperture region, with the noticeable exception of NGC 4501 and NGC 4698. This last Sa galaxy shows the presence of a stellar (Bertola et al. 1999) and gaseous (Bertola & Corsini 2000) core with an angular momentum perpendicular to that of the main galactic disk. This core can be identified as a disk from *HST* imaging (Scarlata et al. 2001). Consistent with these findings, a recent accretion event may explain why NGC 4698 is one of the two galaxies, among our sample of 16, to exhibit a strongly asymmetric gas distribution within $0\farcs3$ (± 6 rows) where, assuming that the nuclear regions of our galaxies are dominated by SMBHs with masses consistent with the M_{BH}-σ_* relation, the dynamical timescale ranges from 0.5 to 12.0 Myr.

TABLE 2

RESULTS OF THE ROTATING DISK MODEL

Galaxy Name (1)	σ_{flux} (arcsec) (2)	$\sigma_{\mathrm{flux,corr}}$ (arcsec) (3)	$M_{\mathrm{BH}}(\Phi = \Phi_{\mathrm{BH}})$ ($M_\odot$) (4)	$M_{\mathrm{BH}}(\Phi = \Phi_{\mathrm{BH}} + \Phi_*)$ ($M_\odot$) (5)	M_{BH}(Sensitivity Limit) ($M_\odot$) (6)
NGC 2787......	0.056	0.053	1.9×10^8	1.8×10^8	3.8×10^6
NGC 3351......	0.132	0.153	9.7×10^6	8.0×10^6	2.1×10^6
NGC 3368......	0.086	0.095	3.8×10^7	2.7×10^7	4.5×10^6
NGC 3982......	0.051	0.046	8.0×10^7	7.5×10^7	3.3×10^6
NGC 3992......	0.051	0.046	5.7×10^7	5.3×10^7	3.0×10^6
NGC 4143......	0.035	0.024	1.4×10^8	1.4×10^8	1.4×10^6
NGC 4203......	0.030	0.015	2.3×10^7	2.3×10^7	4.3×10^5
NGC 4321......	0.046	0.040	2.7×10^7	2.5×10^7	2.3×10^6
NGC 4450......	0.046	0.040	1.1×10^8	1.1×10^8	3.1×10^6
NGC 4459......	0.041	0.033	1.3×10^8	1.3×10^8	2.9×10^6
NGC 4477......	0.056	0.053	8.7×10^7	7.8×10^7	5.1×10^6
NGC 4501......	0.081	0.088	9.0×10^7	7.4×10^7	7.6×10^6
NGC 4548......	0.066	0.067	3.3×10^7	2.8×10^7	3.8×10^6
NGC 4596......	0.056	0.053	1.1×10^8	9.4×10^7	5.6×10^6
NGC 4698......	0.091	0.100	8.0×10^7	7.1×10^7	6.0×10^6
NGC 4800......	0.076	0.081	3.2×10^7	2.0×10^7	6.1×10^6

NOTE.—Col. (1): Galaxy name. Col. (2): Derived first guess of the intrinsic flux extent (see § 3.2). Col. (3): Adopted intrinsic flux extent (see § 3.2). Col. (4): Upper limit on M_{BH} (1 σ) obtained with a rotating disk model ignoring the stellar gravitational potential (§ 3.2). Col. (5): Upper limit on M_{BH} (1 σ) obtained with a rotating disk model including the stellar gravitational potential (§ 3.2). Col. (6): Sensitivity limit to M_{BH}.

quently the velocity dispersions σ_{ap} are almost equal to the ones obtained with perfectly centered apertures (when $\bar{v}_{ap} \equiv 0$).

For comparison, we also show the stellar surface brightness profiles in Figure 1, derived from the stellar continuum in the spectra; this comparison justifies our assumption that the gas and the stellar distribution are concentric. Indeed, an independent fit to the stellar profiles with the same functional profile adopted for the gas ones led to a mean offset along the slit direction of only 0.08 ± 0.17 pixels, consistent with no offset at all.

As an intermediate result of our modeling, we show in Figure 2 the $\sigma_{ap}/v_c(R_{ref})$ ratios obtained in a Keplerian potential for different disk orientations and a range of typical values for σ_{flux}; the predicted σ_{ap} does not depend on the total flux or a_{flux}. The predicted central line width obviously increases from face-on to edge-on systems. At a given disk orientation, models with intrinsically more concentrated gas emissivity always have a larger line width than those with more extended flux distributions because the gas resides at smaller radii. Since the central $0\rlap{.}''25 \times 0\rlap{.}''2$ aperture is nearly square, the impact of the position angle parameter ϕ on the final confidence limits for the $\sigma_{ap}/v_c(R_{ref})$ ratio is negligibly small.

The flux distributions in our sample galaxies are concentrated enough that the predicted line widths are *monotonically* decreasing with increasing cos i. Since randomly oriented disks have uniformly distributed cos i, we can use Figure 2 to derive the median values and 68% upper and lower confidence limits for the M_{BH}, respectively, by simply taking the values of $\sigma_{ap}/v_c(R_{ref})$ for the models with cos $i = 0.5, 0.84$, and 0.16.

There is a minor practical complication in this modeling: while changing the orientation of a disk with a fixed intrinsic flux distribution, the predicted flux profile along each of the five $0\rlap{.}''05 \times 0\rlap{.}''2$ apertures within the central $0\rlap{.}''25 \times 0\rlap{.}''2$ aperture changes, eventually becoming inconsistent with

the observed one. Hence, at any given disk orientation we must readjust the intrinsic flux concentration σ_{flux} in order to match the central five flux data points. Such a correction is particularly important for highly inclined disks, which have very different flux profiles when considered at different position angles. Since our M_{BH} upper limits are derived for nearly face-on orientations, these corrections will not strongly affect our results. Furthermore, tests have shown that the induced scatter in the $\sigma_{ap}/v_c(R_{ref})$ ratio at any given inclination is considerably smaller than the face-on to edge-on variation.

For simplicity, we only used a statistical correction for this effect. For a set of intrinsic values $\sigma_{flux,in}$, we collected all the central flux profiles predicted for a uniform grid in cos i and ϕ. Then we treated each of these profiles as observed ones and matched each of them with a PSF-convolved Gaussian profile to get a distribution of $\sigma_{flux,out}$ values and a median $\langle\sigma_{flux,out}\rangle$ value for each $\sigma_{flux,in}$. By comparing the median $\langle\sigma_{flux,out}\rangle$ values with the corresponding $\sigma_{flux,in}$ values (Fig. 3), we can correct for each galaxy our initial guess of the intrinsic σ_{flux}, derived by matching the observed central flux profiles of Figure 1. For a given galaxy the corrected flux concentration to be input into the models is characterized by the $\sigma_{flux,in}$ value that, according to the previous scheme, leads to a median $\langle\sigma_{flux,out}\rangle$ equal to the σ_{flux} of that galaxy. This $\sigma_{flux,in}$ value describes the intrinsic flux distribution that, when considering different disk orientations, leads to the predicted flux profiles that are the most consistent with the observed one for the given galaxy. We call these particular $\sigma_{flux,in}$ for each galaxy the corrected $\sigma_{flux,corr}$ values, which we list in Table 2 along with the (1 σ) upper limits on M_{BH} obtained adopting them.

FIG. 3.—Correction function for the derived flux concentrations. The solid line relates each intrinsic $\sigma_{flux,in}$ with the median $\langle\sigma_{flux,out}\rangle$ of all the $\sigma_{flux,out}$ values that well matched the flux profiles obtained from each $\sigma_{flux,in}$, as described in § 3.2. Correspondingly, for each sample galaxy, the open circles relate each of the σ_{flux} obtained by matching the galaxy flux profiles of Fig. 1 with the intrinsic flux concentration $\sigma_{flux,corr}$ that need to be input into the models. The identity transformation (*dashed line*) is shown for comparison.
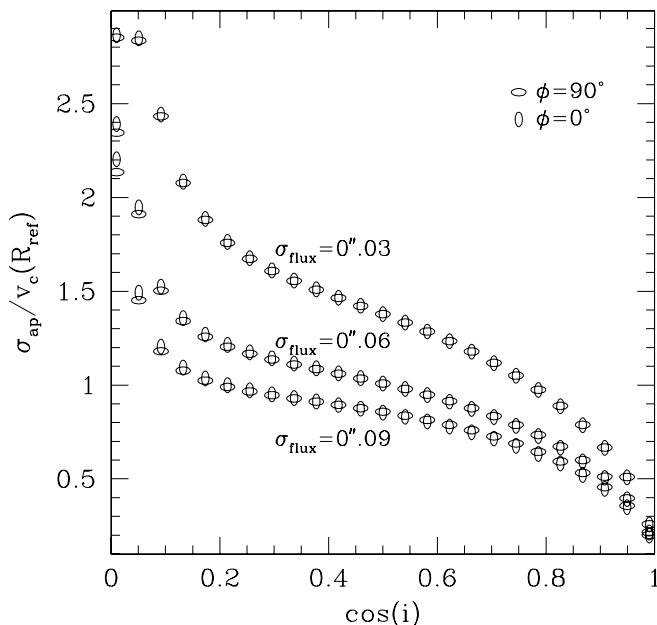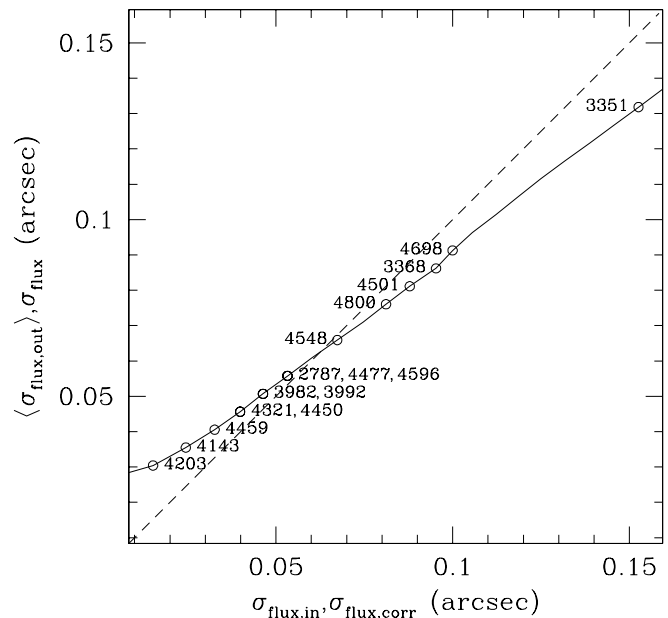

FIG. 2.—Predicted ratio of the gas central velocity dispersion to the circular velocity at the reference radius, as obtained by the Keplerian disk modeling (§ 3.2) for different disk inclinations, position angles ϕ, and intrinsic flux distributions.

As a final remark we notice that at the mean distance of our sample galaxies (~ 15 Mpc) and considering the typical mass of their central SMBHs ($\sim 2.4 \times 10^7 M_\odot$, as predicted by the $M_{\rm BH}$-σ_* relation), the adopted intrinsic flux distributions are generally concentrated enough that a double-horned LOSVD should be expected, especially for highly inclined disks. The fact that such a feature is not found in the observed emission-line profiles could represent evidence of an intrinsic turbulence in the gas. Indeed, when the full LOSVD is properly constructed (by collecting at each velocity bin the total flux within the $0\rlap{.}''25 \times 0\rlap{.}''2$ aperture that arises from the corresponding isovelocity slice of the flux distribution, once convolved with the STIS PSF), the double-horned shape disappears when an intrinsic gas velocity dispersion is introduced. In the favorable case, within this context, of a nearly face-on disk with $\cos i = 0.84$, a velocity dispersion of about ~ 30 km s^{-1} would be required on average to smooth the double-horned shape, thus increasing the predicted line widths by 9% and decreasing the derived upper limits on $M_{\rm BH}$ by 19%. Too many assumptions will be required to make this correction on the case-by-case basis and would probably require direct fitting of the observed emission lines, as done by Barth et al. (2001b). By adopting our current approach, our limits on $M_{\rm BH}$ remain conservative upper bounds.

3.3. The Stellar Contribution

We now proceed to evaluate the impact of the stellar potential Φ_* on our modeling. We start by estimating for each galaxy the expected radius of the "sphere of influence" of the SMBH, $r_{\rm infl} = GM_{\rm BH}/\sigma_*^2$, within which $M_{\rm BH}$ dominates the dynamics of a galaxy with a stellar velocity dispersion σ_*. For this estimate we adopt the $M_{\rm BH}$-σ_* relation as parameterized by Gebhardt et al. (2000a), $\log M_{\rm BH} = 3.75 \log \sigma_* - 0.55$. Then, $\log r_{\rm infl} = 1.75 \log \sigma_* - 2.92$, where $M_{\rm BH}$ is in units of $M_\odot$, σ_* in km s^{-1}, and $r_{\rm infl}$ in pc. In Figure 4 we compare $r_{\rm infl}$ with the physical scale corresponding to the mean radius of our central aperture $R_{\rm aperture} = [(0\rlap{.}''25 \times 0\rlap{.}''2)/\pi]^{1/2} \approx 0\rlap{.}''13$ and find that for many of our galaxies $r_{\rm infl} \leq R_{\rm aperture}$, indicating that the stellar mass M_* within $R_{\rm aperture}$ is comparable to or exceeds $M_{\rm BH}$. Therefore, our analysis needs to account for the stellar mass, and we need to derive the stellar mass density profiles $v_*(r)$, in particular for galaxies with smaller σ_*.

The relative importance of M_* and $M_{\rm BH}$ on the central line width depends also on the spatial extent of the gas emissivity. In particular, even when $r_{\rm infl} < R_{\rm aperture}$, the presence of the SMBH can still be noticed from the observed $\sigma_{\rm cen}$ if $\sigma_{\rm flux} \approx r_{\rm infl}$, that is, if most of the collected flux within $R_{\rm aperture}$ was emitted by gas moving on nearly Keplerian orbits. Further, the impact of Φ_* on the predicted $\sigma_{\rm ap}$ also decreases with increasing flux concentration since in general the circular velocity curve due to the stars increases monotonically with the distance from the galactic center. Indeed the central slope of stellar density profiles can be represented by a power law $v_*(r) \sim r^{-\alpha}$ with $\alpha \leq 2$ (Gebhardt et al. 1996). Figure 4 shows that $\sigma_{\rm flux}$ is in general smaller than $R_{\rm aperture}$, and we expect that the inclusion of the stellar mass in our modeling will cause only a modest correction in the black hole masses inferred in § 3.2.

To quantify the stellar mass contribution in each galaxy, we derived the mass density profile $v_*(r)$ by deprojecting the stellar surface brightness distribution $\Sigma_*(R)$ obtained from the STIS acquisition image, assuming spherical symmetry
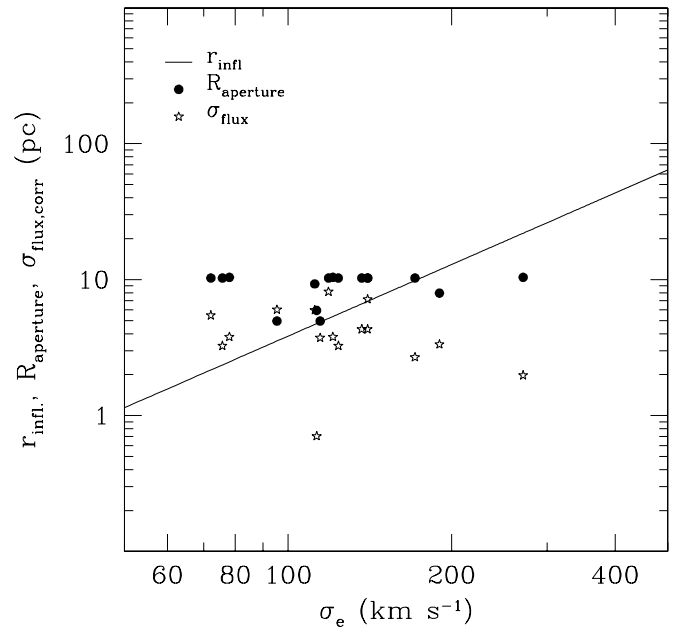

FIG. 4.—Physical dimension of the region subtended by our central $0\rlap{.}''25 \times 0\rlap{.}''2$ aperture (*filled circles*) and flux distribution extent of our sample galaxies (*open stars*) compared to the "sphere of influence" radius of SMBHs consistent with the $M_{\rm BH}$-σ_* relation (*solid line*).

and a constant mass-to-light ratio Υ. We applied the same multi-Gaussian algorithm adopted in S01 to circularly averaged $\Sigma_*[(ab)^{1/2}]$ surface brightness profiles, extracted using the IRAF task ELLIPSE and color corrected into Johnson R-band magnitudes using the IRAF package SYNPHOT and assuming E–S0 galaxy templates. Gaussian components with $\sigma \leq 0.5$ pixels were considered as unresolved point sources and hence were excluded from the stellar mass budget. For simplicity we adopted for all galaxies $\Upsilon = 5$ $M_\odot/L_\odot$, rescaled from van der Marel (1991) for $H_0 = 75$ km s^{-1} Mpc^{-1}, instead of deriving individual values for Υ by matching ground-based σ_* measurements (see S01).

Including the stellar potential in the modeling results in a 27% reduction of the median black hole masses (for $\cos i = 0.5$) needed to explain the observed central line widths. Nonetheless, this effect is important for galaxies with small σ_* values; the median $M_{\rm BH}$ decreased by 37% for the sample galaxies with the lowest σ_* (NGC 3982, NGC 4321, and NGC 4548) but only by 3% for the ones with the highest σ_* (NGC 4143).

The impact of the stellar mass on the upper limits of the black hole mass, which are central to our analysis, is yet smaller, on average less than 12% (see Table 2). Indeed, similar to the purely Keplerian case, the predicted central line widths are always found to be increasing monotonically with disk inclination, such that the derived 1 σ upper limits on $M_{\rm BH}$ are obtained here also from models with nearly face-on disks. In this situation the circular velocities needed by the model to explain the observed line widths always by far exceed the ones provided only by the stellar potential.

3.4. Gas in Hydrostatic Equilibrium

So far we have assumed that the observed central line widths are due to pure orbital motion of gas in a disk around the galaxy center. But even if we ignore non-gravitational effects, we still need to investigate how much the derived $M_{\rm BH}$ upper limits depend on different choices

for the kinematic behavior of the ionized gas. In particular, it is conceivable that the gas is at least in part supported by gas pressure. In order to explore the impact of such pressure on our results, we considered the extreme case of pure hydrostatic support. For any emissivity density profile ρ, we need only the second LOSVD velocity moment Σv^2 without streaming motions. We obtain this moment by solving the hydrostatic equilibrium equation $d(\rho\sigma^2)/\rho \, dr = -d\Phi/dr$ for the gas velocity dispersion $\sigma(r)$ and then by integrating the luminosity-weighted σ along the line of sight.

Under these assumptions, we proceeded to match the observed σ_{cen} for all the galaxies, assuming Gaussian profiles for their emissivity densities ρ, whose width has to match the observed central flux profiles. We thus obtained for each galaxy a value for the mass of the putative SMBH, in a purely Keplerian potential.

From this exercise we found that the predicted central velocity dispersions σ_{ap} correspond to values from the rotating disk model with disk inclinations always between 0.65 and 0.71. Consequently, the M_{BH} values inferred by considering hydrostatic equilibrium lie within the $\pm 1\,\sigma$ confidence limits obtained from the rotating disk models, and all previous results hold.

4. RESULTS

We have explored the dynamical implications of the observed emission-line widths arising from the central ~ 10 pc of our sample galaxies, and we have demonstrated that the most conservative $1\,\sigma$ upper limits of M_{BH} are obtained assuming that the gas resides in a nearly face-on disk ($i \sim 33°$; $\cos i = 0.84$) moving in circular orbits around a central SMBH. Fortunately, extremely face-on orientations are statistically rare.

In Figure 5 we place our M_{BH} upper limits derived for the Keplerian case (§ 3.2) in the M_{BH}-σ_* plane. For a comparison with the M_{BH}-σ_* relation (as parameterized by Gebhardt et al. 2000a) we need to scale each σ_* to σ_e, the value that would have been observed within a circular aperture of $R = R_e$. The proper computation of such a quantity, which should include the contribution from the rotation, was not possible for all the galaxies in our sample, since the necessary combination of surface brightness, velocity dispersion, and rotation velocity radial profiles was not available from the literature for all objects. The only choice in this case is to use the algorithm of Jørgensen, Franx, & Kjaergaard (1995), which was derived on the basis of kinematical data for 51 elliptical and lenticular galaxies and which also accounts for the effect of rotation. For the effective radii we adopted the seeing-corrected values from Baggett, Baggett, & Anderson (1998). In the few cases in which this last compilation did not provide R_e measurements (NGC 3982 and NGC 4800), we assumed $\sigma_e = \sigma_*$. The σ_e values are listed in Table 2.

Figure 5 shows that, with one exception (NGC 4143), our derived upper limits on M_{BH} lie within the scatter of the M_{BH}-σ_* relation or above it. In this sense, the proposed M_{BH}-σ_* relation passes this observational test for more than a dozen objects. Furthermore, except for the three galaxies with the lowest value of σ_*, our upper limits on M_{BH} exceed the values predicted by the M_{BH}-σ_* relation only by a modest amount (in average by a factor of ~ 4.6).

In particular for the galaxies in our sample with actual M_{BH} measurements from spatially resolved kinematics (S01), the present upper limits are consistent, within the
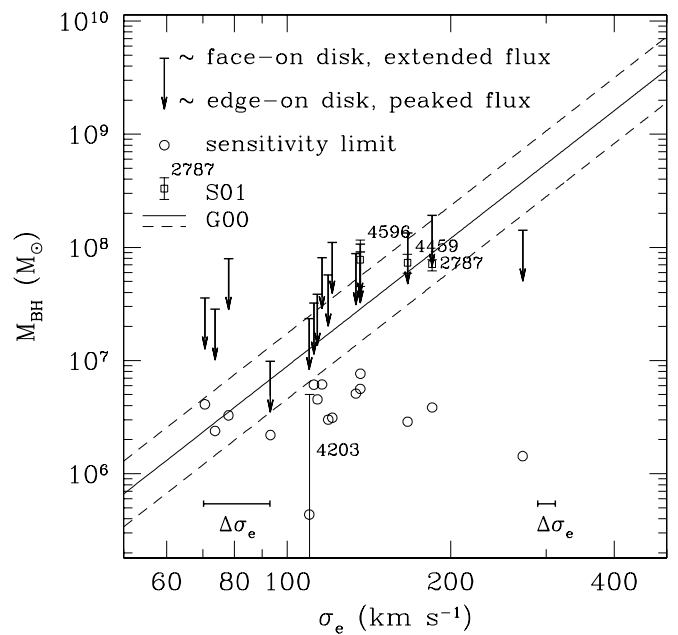

FIG. 5.—M_{BH} upper limits in the M_{BH}-σ_* relation. The 1 σ upper limits on M_{BH} (*thick downward-pointing arrows*) obtained by the Keplerian disk modeling (§ 3.2) are compared with the range of black hole masses expected as a function of σ_* from the M_{BH}-σ_* relation and its absolute scatter in M_{BH} (*solid and dashed lines*; from Gebhardt et al. 2000a). The open squares show the M_{BH} measurements obtained from extended kinematics in four of our sample galaxies by S01, while the open circles represent the sensitivity limit of our experiment for each sample galaxy. The thick horizontal error bars indicate how the mean error on σ_* for our sample would appear in the right and left of the plot.

errors, with the published M_{BH} values. Moreover, when our 1 σ upper limits are compared with other published M_{BH} measurements (as compiled recently by Kormendy & Gebhardt 2001; Fig. 6), most appear to be quite close to the actual values for the black hole mass, with the exception of the same galaxy lying below the M_{BH}-σ_* relation (NGC 4143) and the three objects in our sample with the lowest value of σ_* (NGC 3982, NGC 4321, and NGC 4548). Figure 6 therefore shows that for the bulk of our sample with $100 \le \sigma_* \le 200$ km s^{-1} our line width modeling technique gives results statistically consistent with the values obtained through other techniques.

The current data do not provide any indication that the spiral and lenticular galaxies in our sample differ in their black hole masses. Further, our upper limits on M_{BH} do not seem to differ between barred or unbarred host galaxies, or as a function of the nuclear spectral classification.

For any interpretation of upper limits, the basic sensitivity of the experiment is crucial. Our M_{BH} sensitivity limit depends not only on the physical size of the resolution element and on the amount of stellar mass but also on the spatial emissivity distribution of the gas. Indeed, we often find the spatial extent of the ionized gas to be smaller than the dimension of the 0″.25 × 0″.2 aperture. Considering the spatial emissivity of each of our sample galaxies, we can derive conservative sensitivity limits for a nearly face-on disk ($\cos i = 0.84$) by first computing the predicted line widths arising in a purely stellar potential, and then by asking what values of M_{BH} need to be added in order to increase those line widths by their typical measurement error, conservatively ~ 10 km s^{-1} (see § 2.3).
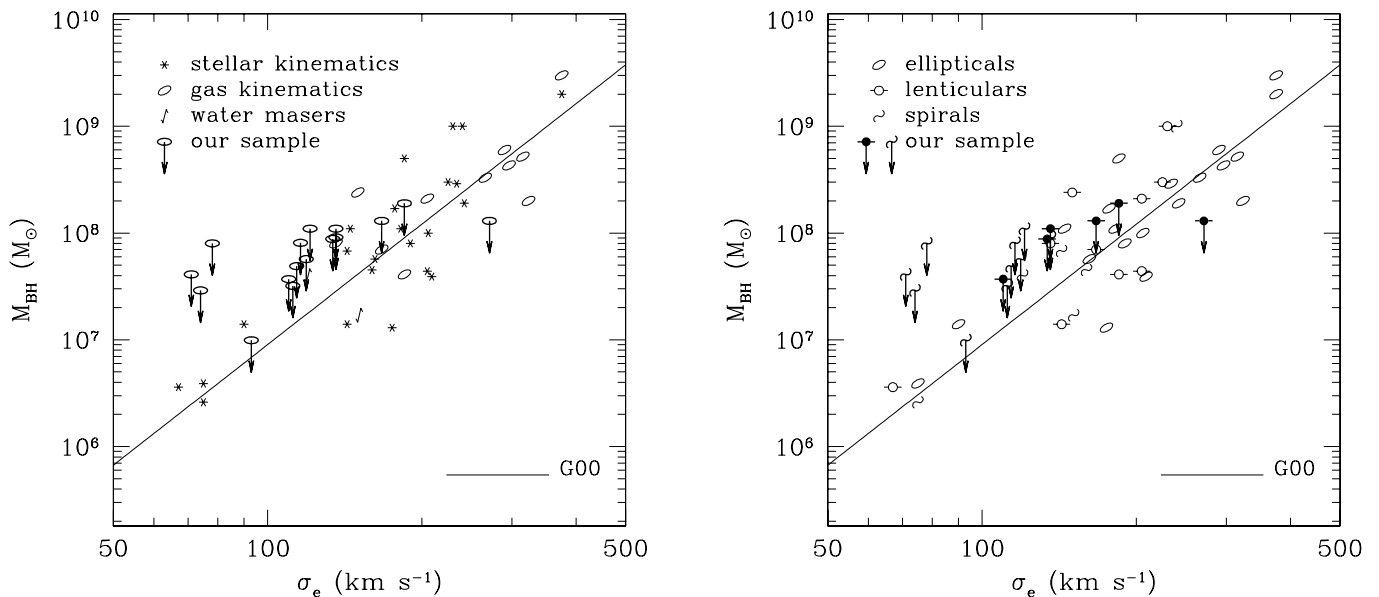
FIG. 6.—M_{BH} upper limits vs. M_{BH} determinations. In both panels the M_{BH} upper limits for our sample galaxies (*symbols with downward-pointing arrows*) are compared with the M_{BH} determinations that were deemed accurate in the recent compilation of Kormendy & Gebhardt (2001) (*symbols without arrows*). To be consistent with this compilation, for our sample objects with measured surface brightness fluctuation distance moduli (Tonry et al. 2001; for NGC 2787, NGC 3368, NGC 4143, NGC 4203, NGC 4459, and NGC 4548) the M_{BH} upper limits have been rescaled assuming these distances. In the left panel the different symbols stand for the different techniques used to measure the M_{BH}, while in the right panel they represent the different types of host galaxies. The solid lines show the M_{BH}-σ_* relation as compiled by Gebhardt et al. (2000a).

With a mean value of $3.9 \times 10^6\ M_\odot$, the derived sensitivity limits lie well below the inferred $1\ \sigma$ upper limits on M_{BH} (see Fig. 5 and Table 2), which can therefore be considered robust. We notice that by assigning a constant mass-to-light ratio to *all* Gaussian components of the luminosity density profile, including the ones with $\sigma \leq 0.5$ pixels (see § 3.3), the derived sensitivity limits increase only by 30%, to a mean value of $5.1 \times 10^6\ M_\odot$.

Our $1\ \sigma$ upper limits for the whole sample correspond to M_{BH} values produced by nearly face-on disks (cos $i = 0.84$). As mentioned, we find one object, NGC 4143, for which the derived upper limit on M_{BH} is below the M_{BH}-σ_* relation. For 16 sample members, the expected number of disks with inclinations more face-on than cos $i = 0.84$ is ~ 2–3. In order to reconcile the observed central line width of NGC 4143 with the M_{BH}-σ_* relation within the Keplerian disk framework, the disk would need to have an inclination angle of 27°. However, it should be noticed that NGC 4143 is among our sample one of the galaxies with a nearly unresolved spatial emissivity distribution (see Fig. 1), which could actually be more concentrated than the one adopted by us. Since this would lower the upper limit on M_{BH}, we think that NGC 4143 represents an interesting candidate for future investigations.

The situation is different for the three galaxies with the lowest values of σ_* in our sample because their spatial flux profiles are resolved. Hence, we cannot explain their relatively high values of σ_{cen} (~ 100 km s^{-1}) within the context of a Keplerian disk in terms of gas orbiting in the vicinity of an $\sim 2 \times 10^6\ M_\odot$ SMBH (as predicted by the M_{BH}-σ_* relation). Furthermore, as the derived sensitivity limits on M_{BH} for these three galaxies are also around $\sim 2 \times 10^6\ M_\odot$ (see Table 2), we cannot expect the stellar mass contribution to help explain their σ_{cen} values. Indeed, the line widths obtained from the stellar potential *and* a $2 \times 10^6\ M_\odot$ SMBH are considerably smaller than the observed ones.

The predicted line widths in this case are for these three galaxies in average ~ 40 and ~ 75 km s^{-1}, in the nearly face-on (cos $i = 0.84$) and edge-on (cos $i = 0.16$) case, respectively. Alternatively, the observed central line widths might arise in all three objects from highly inclined nuclear disks. This is not only unlikely but may also be insufficient, as in the case of NGC 3982, even when considering a perfectly edge-on nuclear disk. Therefore, in the case of the three less massive bulges, we may have indirect evidence that at least part of the observed line width is due to non-gravitational effects.

5. DISCUSSION AND CONCLUSIONS

We have demonstrated that with *HST*'s spatial resolution the integrated line widths of the central emission lines provide stringent and interesting constraints on the presence of SMBHs. The relative observational ease of this approach makes it potentially applicable to large galaxy samples, which would allow us to test the universal applicability of the emerging relations between M_{BH} and galaxy properties.

Our modeling, which was necessary to connect the observed σ_{cen} with the quantity of immediate interest, $v_c(R_{ref})$, was based on the assumption that the gas line width arises solely from orbital motion within a randomly oriented disk around a putative SMBH.

Reality is undoubtedly more complex, and we have considered other potentially relevant effects, such as the stellar contribution to the total gravitational potential and, more simplistically, hydrostatic support of the gas. The dynamical influence of outflows and magnetic fields could also be important. Except for fine-tuned circumstances, all these effects will provide an additional contribution to the observed line width and the inferred upper limit on M_{BH} will be tighter. Hence, our adopted set of assumptions lead to conservative estimates. Comparison of our upper limits

with direct $M_{\rm BH}$ determinations, either statistically (Fig. 6) or in a few cases individually (Fig. 5), showed that our 1 σ upper limits are generally near the actual value of $M_{\rm BH}$.

We have applied this analysis to a set of 16 galaxies whose sample selection was not biased toward particular $M_{\rm BH}$ values. Remarkably, with one exception, our 1 σ upper limits on $M_{\rm BH}$ closely parallel the $M_{\rm BH}$-σ_* relation and suggest that for galaxies with $\sigma_* \geq 100$ km s^{-1}, SMBHs with exceptionally high $M_{\rm BH}$ that violate the $M_{\rm BH}$-σ_* relation must be rare. By considerably broadening the range of host galaxies surveyed for SMBHs, our 16 upper limits further support the emerging picture wherein the black hole mass and the overall galaxy structure are closely linked.

Even with a limited sample of 16 objects, we have been able to isolate a few cases worthy of further investigations. NGC 4143 stands out as the only object that falls below the $M_{\rm BH}$-σ_* relation; we speculate that this may indicate that its

nuclear disk is nearly face-on. Three low-σ_* galaxies (NGC 3982, NGC 4321, and NGC 4548) seem to have $M_{\rm BH}$ upper limits that lie systematically offset from other galaxies of low-velocity dispersion in which the $M_{\rm BH}$ was obtained by studying the stellar kinematics. This suggests that in low-mass bulges nongravitational forces can considerably affect the gas motions in the central 10 pc.

REFERENCES

Baggett, W. E., Baggett, S. M., & Anderson, K. S. J. 1998, AJ, 116, 1626
Barth, A. J., Sarzi, M., Rix, H.-W., Ho, L. C., Filippenko, A. V., & Sargent, W. L. W. 2001a, ApJ, 555, 685
———. 2001b, in ASP Conf. Ser. 249, The Central Kpc of Starbursts and AGN: The La Palma Connection, ed J. H. Knapen et al. (San Francisco: ASP), 370
Bertola, F., & Corsini, E. M. 2000, in ASP Conf. Ser. 197, Dynamics of Galaxies: From the Early Universe to the Present, ed. F. Combes, G. A. Mamon, & V. Charmandari (San Francisco: ASP), 115
Bertola, F., Corsini, E. M., Beltrán, J. C. V., Pizzella, A., Sarzi, M., Cappellari, M., & Funes, S. J. 1999, ApJ, 519, L127
Bower, G. A., et al. 1998, ApJ, 492, L111
Corsini, E. M., et al. 1999, A&A, 342, 671
Cretton, N., & van den Bosch, F. C. 1999, ApJ, 514, 704
Dalle Ore, C., Faber, S. M., Jesus, J., Stoughton, R., & Burstein, D. 1991, ApJ, 366, 38
de Vaucouleurs, G., de Vaucouleurs, A., Corwin, H. G., Jr., Buta, R. J., Paturel, G., & Fouqué, R. 1991, Third Reference Catalogue of Bright Galaxies (New York: Springer)
Di Nella, H., Garcia, A. M., Garnier, R., & Paturel, G. 1995, A&AS, 113, 151
Dressler, A., & Richstone, D. O. 1988, ApJ, 324, 701
Eckart, A., & Genzel, R. 1997, MNRAS, 284, 576
Ferrarese, L., Ford, H. C., & Jaffe, W. 1996, ApJ, 470, 444
Ferrarese, L., & Merritt, D. 2000, ApJ, 539, L9
Ferrarese, L., Pogge, R. W., Peterson, B. M., Merritt, D., Wandel, A., & Joseph, C. L. 2001, ApJ, 555, L79
Filippenko, A. V., & Sargent, W. L. W. 1985, ApJS, 57, 503
Gebhardt, K., et al. 1996, AJ, 112, 105
———. 2000a, ApJ, 539, L13
———. 2000b, ApJ, 543, L5
Genzel, R., Eckart, A., Ott, T., & Eisenhauer, F. 1997, MNRAS, 291, 219
Ghez, A. M., Klein, B. L., Morris, M., & Becklin, E. E. 1998, ApJ, 509, 678
Harms, R. J., et al. 1994, ApJ, 435, L35
Héraudeau, Ph., & Simien, F. 1998, A&AS, 133, 317
Héraudeau, Ph., Simien, F., Maubon, G., & Prugniel, P. 1999, A&AS, 136, 509
Herbst, T. M., Beckwith, S. V. W., Forrest, W. J., & Pipher, J. L. 1993, AJ, 105, 956
Ho, L. C. 1999, in Observational Evidence for Black Holes in the Universe, ed. S. K. Chakrabarti (Dordrecht: Kluwer), 157
Ho, L. C., Filippenko, A. V., & Sargent, W. L. W. 1995, ApJS, 98, 477
———. 1997, ApJS, 112, 315
Ho, L. C., Rudnick, G., Rix, H.-W., Shields, J. C., McIntosh, D. H., Filippenko, A. V., Sargent, W. L. W., & Eracleous, M. 2000, ApJ, 541, 120

Jarvis, B. J., Dubath, P., Martinet, L., & Bacon, R. 1988, A&AS, 74, 513
Jørgensen, I., Franx, M., & Kjaergaard, P. 1995, MNRAS, 276, 1341
Kaspi, S., Smith, P. S., Netzer, H., Maoz, D., Jannuzi, B. T., & Giveon, U. 2000, ApJ, 533, 631
Kauffmann, G., & Haehnelt, M. 2000, MNRAS, 311, 576
Kent, S. M. 1990, AJ, 100, 377
Kormendy, J., et al. 1996a, ApJ, 459, L57
———. 1996b, ApJ, 473, L91
Kormendy, J., & Gebhardt, K. 2001, in The 20th Texas Symposium on Relativistic Astrophysics, ed. H. Martel & J. C. Wheeler (New York: AIP), in press
Kormendy, J., & Richstone, D. 1995, ARA&A, 33, 581
Magorrian, J., et al. 1998, AJ, 115, 2285
Maoz, E. 1995, ApJ, 447, L91
———. 1998, ApJ, 494, L181
Miyoshi, M., Moran, J., Herrnstein, J., Greenhill, L., Nakai, N., Diamond, P., & Inoue, M. 1995, Nature, 373, 127
Nelson, C. H., & Whittle, M. 1995, ApJS, 99, 67
Oke, J. B., & Gunn, J. E. 1982, PASP, 94, 586
Rix, H.-W., Kennicutt, R. C., Jr., Braun, R., & Walterbos, R. A. M. 1995, ApJ, 438, 155
Rudnick, G., Rix, H.-W., & Kennicutt, R. C., Jr. 2000, ApJ, 538, 569
Salucci, P., Ratnam, C., Monaco, P., & Danese, L. 2000, MNRAS, 317, 488
Sarzi, M., Rix, H.-W., Shields, J. C., Rudnick, G., Ho, L. C., McIntosh, D. H., Filippenko, A. V., & Sargent, W. L. W. 2001, ApJ, 550, 65 (S01)
Scarlata, M. C., Bertola, F., Cappellari, M., Sarzi, M., Corsini, E. M., & Pizzella, A. 2001, in ASP Conf. Ser. 230, Galaxy Disks and Disk Galaxies, ed. J. G. Funes & E. M. Corsini (San Francisco: ASP), 163
Schechter, P. L. 1983, ApJS, 52, 425
Shields, J. C., Rix, H.-W., McIntosh, D. H., Ho, L. C., Rudnick, G., Filippenko, A. V., Sargent, W. L. W., & Sarzi, M. 2000, ApJ, 534, L27
Timmermann, R., Genzel, R., Poglitsch, A., Lutz, D., Madden, S. C., Nikola, T., Geis, N., & Townes, C. H. 1996, ApJ, 466, 242
Tonry, J., Dressler, A., Blakeslee, J. P., Ajhar, E. A., Fletcher, A. B., Luppino, G. A., Metzger, M. R., & Moore, C. B. 2001, ApJ, 546, 681
Tully, R. B. 1988, Nearby Galaxies Catalog (Cambridge: Cambridge Univ. Press)
van der Marel, R. P. 1991, MNRAS, 253, 710
van der Marel, R. P., de Zeeuw, P., Rix, H.-W., & Quinlan, G. D. 1997, Nature, 385, 610
Verdoes Kleijn, G. A., van der Marel, R. P., Carollo, C. M., & de Zeeuw, P. T. 2000, AJ, 120, 1221
Wandel, A., Peterson, B. M., & Malkan, M. A. 1999, ApJ, 526, 579
Whitmore, B. C., Schechter, P. L., & Kirshner, R. P. 1979, ApJ, 234, 68
Yusef-Zadeh, F., Roberts, D. A., & Wardle, M. 1997, ApJ, 490, L83